Multifunctional Nanodiamond Interfacial Layer for Ultra-Stable Zinc-Metal Anodes

Kai Liu, Mingzi Sun, Shuo Yang, Guoqiang Gan, Shuyu Bu, Anquan Zhu, Dewu Lin, Tian Zhang, Chuhao Luan, Chunyi Zhi, Pengfei Wang, Bolong Huang,* Guo Hong,* and Wenjun Zhang*

Achieving reversible plating/stripping of zinc (Zn) anodes is crucial in aqueous Zn-ion batteries (AZIBs). However, undesired dendrite growth and parasitic side reactions severely deteriorate battery lifespan. The construction of stable protective coating is an effective strategy to enhance anode stability. In this study, a multifunctional nanodiamond (ND) inorganic layer is designed and constructed on both Zn and Cu electrodes that can both effectively inhibit dendrite growth and suppress Zn anode corrosion. Experimental results and theoretical calculations demonstrate that this artificial protective layer, with ultra-high surface energy, enables the controlled creation of abundant nucleation sites (in the order of 10^{12} cm^{-2}) for the homogenization of ion flux and electric field on the anode. It is found that zinc ions preferentially adhere to the diamond surfaces with lower diffusion barriers, leading to uniform zinc deposition. A symmetric cell with the ND-protected Zn (Zn-ND) anode exhibits reversible plating/stripping behavior for an impressive duration of over 3600 h at 1 mA cm^{-2}. Furthermore, the MnO$_2$||Zn full battery retains 90% of its initial capacity after 3500 cycles at 2 A g^{-1}, and assembled hybrid capacitor operates smoothly over 65 000 cycles at 10 A g^{-1}. These results underscore the potential of this coating as a promising solution for achieving highly stable Zn anodes for aqueous batteries.

1. Introduction

The increasing demands for energy storage systems have spurred extensive research into the development of safe and high-performance battery technologies. Aqueous zinc-ion batteries (AZIBs) hold great promise for large-scale energy storage applications due to their high safety and cost-effectiveness.[1] However, their practical application is constrained by multiple challenges, including excessive dendrite growth, slow deposition kinetics, and inherent chemical corrosion accompanied by hydrogen evolution reactions (HER). These factors limit the further utilization of zinc metal anodes and result in poor electrochemical stability in aqueous electrolytes.[2] The growth of zinc dendrites involves several stages, including the migration of Zn^{2+} from electrolyte to anode, electrochemical redox, chemical and physical structure evolutions at the anode–electrolyte interphase.[3] Consequently, considerable efforts have been made to suppress dendrite formation, mitigate parasitic side reactions at the interfaces, and enhance the electrodeposition kinetics, through strategies such as anode structural design,[4] intrinsic structural engineering,[5] surface artificial coating technology,[6] electrolyte modification,[7] and separator design.[8] Among these strategies, surface coating engineering of Zn anodes, using solvent casting method, has proven effectively in protecting Zn anode from corrosion. This approach physically insulated the Zn anode from the acidic

K. Liu, G. Gan, S. Bu, A. Zhu, D. Lin, T. Zhang, C. Luan, G. Hong, W. Zhang
Department of Materials Science and Engineering & Center of Super-Diamond and Advanced Films (COSDAF)
City University of Hong Kong
83 Tat Chee Avenue, Hong Kong, SAR 999077, China
E-mail: guohong@cityu.edu.hk; apwjzh@cityu.edu.hk

M. Sun, B. Huang
Department of Applied Biology and Chemical Technology
The Hong Kong Polytechnic University
Hung Hom, Kowloon, Hong Kong, SAR 999077, China
E-mail: bhuang@polyu.edu.hk

S. Yang, C. Zhi
Department of Materials Science and Engineering
City University of Hong Kong
83 Tat Chee Avenue, Hong Kong, SAR 999077, China

P. Wang
Key Laboratory of Photochemical Conversion and Optoelectronic Materials
Technical Institute of Physics and Chemistry
Chinese Academy of Sciences
Beijing 100190, China

**ADVANCED
SCIENCE NEWS**

www.advancedsciencenews.com

**ADVANCED
ENERGY
MATERIALS**

www.advenergymat.de

electrolyte and promoted the homogeneous nucleation and growth of Zn deposition. The advantage of this ex situ solvent casting strategy lies in its universality for modifying Zn anodes with various functional coatings, without the need to address the issue of additives dispersion in electrolyte. Several types of functional coatings have been developed so far, including metal oxides,[6e,9] polymers,[10] alloy,[5a] carbon materials,[11] and MXenes.[12] However, the formation of Zn dendrites remains an unavoidable issue, both kinetically and thermodynamically. When the balance between Zn deposition and dendrite suppression is disrupted during repeated plating and stripping processes, the Zn dendrites can reappear.[13] Moreover, many existing protection coatings showed low hardness, which makes them susceptible to extensive mechanical distortion during cycling and results in cracks in the coatings. Therefore, it is vital to develop new functional coatings that not only facilitate the uniform distribution of Zn-ions but also maintain the excellent mechanical strength, even after multiple cycles.

The deposition behavior of ions on the anodes is significantly influenced by the surface energy and nucleation site density on anode surface, as well as the diffusion energy of ions.[14] Diamond, a representative member of the carbon family, possesses an sp^3 structure and is well-known for its ultra-high surface energy, highest bulk modulus ($\approx$100 GPa), electrical and chemical inertness, and potential for protecting metal anodes. For example, Cheng et al.[15] used octadecylamine (ODA)-functionalized nanodiamonds (NDs) as an electrolyte additive in lithium hexafluorophosphate ($LiPF_6$) electrolyte to inhibit the growth of lithium dendrites. The preferentially adsorption of Li ions onto the surface of nanodiamond, followed by co-deposition on the anode surface, has been observed. Due to the low diffusion energy barrier of Li ions on nanodiamond, Li ions diffused easier on anode surface, and thus a smooth and even Li plating was achieved. However, the dispersion of functionalized nanodiamond additives in aqueous electrolyte remains a challenge, as the aggregation will accelerate the growth of Zn dendrites during long-term cycling. Liu et al.[16] proposed a double-layered ND via a two-step microwave plasma chemical vapor deposition technology, which effectively reduced the defect density of diamond, ensured excellent mechanical strength and enabled uniform Li deposition. However, the two-step microwave plasma method involves a complex fabrication process and requires expensive equipment. Moreover, the high-temperature synthesis condition for diamond also limits the choice of substrate.

In this study, we have designed and fabricated an interfacial layer of ND on the zinc anode using a blade casting method, employing as a protective anode coating in the aqueous batteries. A stronger preferential adsorption of Zn ions onto the ND surface was observed, compared to the zinc and copper electrode surfaces during Zn plating. The ultrahigh surface energy and lower diffusion energy barrier of ND facilitated the uniform capture of Zn^{2+} ions, leading to the formation of abundant nucleation sites, and the nucleation density for Zn^{2+} could reach up to the order of 10^{12} cm^{-2}. Subsequently, Zn^{2+} was reduced and deposited on the Zn electrode surface under the applied electric field, ensuring high interface stability during zinc deposition and ultimately resulting in dendrite-free Zn deposits beneath the ND layer during plating. Moreover, the ND layer, with its ultra-broad electrochemical stability window and high mechani-

cal strength, ensured outstanding physical and chemical stability during the charge-discharge process. The excellent hydrophilicity of ND coating effectively homogenized the local electric field on the Zn anode surface, thereby suppressing dendrite growth.[16,17] As a result of the multifunctional ND coatings, the Zn-ND anode exhibited an extended cycling of over 3600 h at a moderate current density of 1 mA cm^{-2} and over 1000 h at an high current density of 10 mA cm^{-2}. Moreover, the Zn||ND protected Cu (Cu-ND) battery demonstrated a stable coulombic efficiency of 99.5% after 1100 cycles. Significantly, the assembled Zn-ND||MnO$_2$ battery achieved stable operation for 3500 cycles at 2 A g^{-1} and the Zn-ND||activated carbon (AC) hybrid capacitor displayed an ultralong lifespan of over 65 000 cycles at 10 A g^{-1}, surpassing most of reported results. Density functional theory (DFT) calculations were also used to investigate the mechanism for the ND inorganic layer induced outstanding electrochemical performance. These impressive results highlighted the versatility of the ND layer for highly stable Zn anodes in aqueous electrolytes with simple coating method.

2. Results and Discussion

Figure 1a illustrates the challenges encountered in conventional AZIBs that employ pristine Zn metal anodes. These batteries tend to experience pronounced dendrite growth and HER on the Zn anode surface when operated in acidic electrolytes. Prolonged Zn deposition leads to the accumulation of randomly distributed Zn dendrites, which has the potential to penetrate the separator and cause short-circuiting of batteries. Additionally, the occurrence of severe side reactions contributes to the eventual failure of the battery. To address these issues, the ND artificial coating was introduced on the Zn anodes to improve the reversibility and stability of Zn plating, through preventing the protrusion growth of Zn and the formation of by-products, such as H$_2$ and subsulfates (Figure 1b).[18] The structure of this artificial layer was first characterized by Raman spectroscopy (Figure S1, Supporting Information). The peaks at 1150 cm^{-1} and 1480 cm^{-1} verified the nanocrystalline nature of the commercially produced ND with hydrogen termination. The typical sp^3 characteristic peak of NDs near 1332 cm^{-1} was not found due to their nanocrystalline nature. Because the ND layers were coated on Zn foil through the blade casting of ND and Polyvinylidene Fluoride (PVDF) mixture, their surfaces showed microchannels (Figure 1c). The thickness of the ND coating, as determined by scanning electron microscopy (SEM), was $\approx$5.8 µm (Figure 1d). By adjusting the distance between the Zn foil and the blade during the coating process, the thickness of ND layer could be controlled. SEM images of a thicker coating of 14 µm and a thinner coating of 1.6 µm are presented in Figure S2, Supporting Information. To determine the optimal thickness of the ND layer for effective Zn anode protection, the cycling performance of Zn-ND||Zn-ND symmetric cells with varying ND coating thicknesses were investigated. As shown in Figure S3, Supporting Information, the symmetric cells with the thinnest coating of 1.6 µm experienced premature failure. This can be attributed to brittleness of the relatively thinner ND protection layer, which made it prone to cracking during repeated cycling. The symmetric cell with the thicker ND layer of 14 µm also exhibited limited cycling life, as a short circuit occurred after about 390 h. The increased thickness of the coating
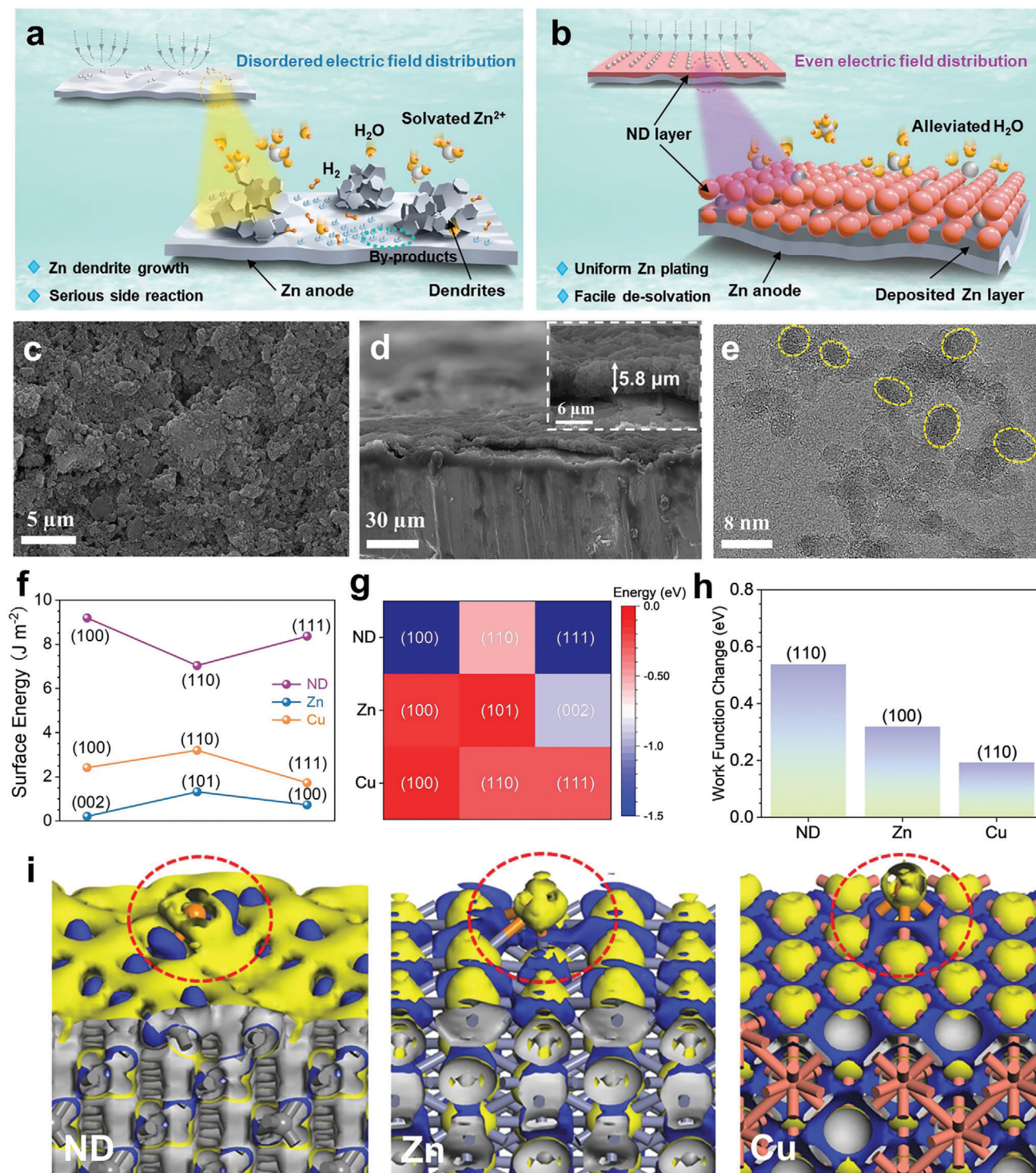
**ADVANCED
SCIENCE NEWS**

www.advancedsciencenews.com

**ADVANCED
ENERGY
MATERIALS**

www.advenergymat.de

Figure 1. a,b) Schematic illustration of Zn deposition on a pristine anode and at interface between ND layer and anode. c) Top-view SEM image of the ND coating on the Zn anode. d) Side-view SEM image of the ND coating, with the inset showing an enlarged area. e) TEM image of ND particles. f) Comparisons of surface energies for ND, Zn, and Cu. g) Binding energy of Zn on different surfaces of ND, Zn, and Cu. h) Changes of the work functions of (110), (100), and (110) surfaces of ND, Zn, and Cu induced by adsorption of Zn. i) Electron density differences of Zn adsorption on (100) surfaces of ND, Zn, and Cu, respectively. Grey balls: C, Dark blue balls: Zn, Pink balls: Cu, Orange balls: adsorbed Zn on the surface. The yellow and blue isosurfaces represent electron depletion and accumulation, respectively.

**ADVANCED
SCIENCE NEWS**

www.advancedsciencenews.com

**ADVANCED
ENERGY
MATERIALS**

www.advenergymat.de

impeded ion transport to anode, resulting in Zn accumulation at the anode surface and eventually breakdown of the Zn anode. However, the Zn anode with a 5.8 µm ND layer demonstrated significantly longer cycling performance compared to the ND layers of 1.6 and 14 µm. This thickness of the ND layer struck a balance, providing effective protection without impeding ion transport. Moreover, the columbic efficiencies (CEs) of Zn||Cu-ND half cells with different ND layer thicknesses were also compared (Figure S4, Supporting Information), and the result were consistent with those of symmetric cells, that is, the ND layer with a thickness of 5.8 µm exhibited the highest stability. Based on these observations, the ND layer with a thickness of 5.8 µm was selected for further research in this study. The transmission electron microscopy (TEM) image in Figure 1e showed that the size of ND particles ranged from 5 to 10 nm. Such cluster size endowed the rich nucleation site of Zn^{2+} for the even deposition behavior (see Supporting Information for details and Scheme S1, Supporting Information).

First-principles calculations were performed to investigate the effectiveness of the ND artificial layer in regulating Zn plating. The surface energies of the low-index surfaces, that is, (100), (110), (111) surfaces of ND and Cu, and (002), (100), (101) surfaces of Zn were calculated, respectively (Figure 1f). Notably, all ND surfaces exhibited much higher surface energies compared to those of both Zn and Cu surfaces. The adsorption energies of Zn on the surfaces of different materials were compared to further understand the impact of surface energies on Zn deposition, (Figure 1g). Considering the nanocrystalline nature and random orientation of NDs, it was evident that ND exhibited much lower overall adsorption energies, indicating a stronger adsorption preference than those on Zn and Cu surfaces. Both (100) and (111) surfaces of ND displayed considerably lower adsorption energies (< −2 eV), supporting the pronounced adsorption tendencies of Zn atoms on the ND surfaces. Furthermore, the changes in work function induced by the adsorption of Zn on the surfaces of ND, Cu, and Zn were investigated to elucidate the interactions between Zn and different surfaces (Figure 1h). The ND, Cu, and Zn surfaces with the lowest free energy, that is, (110) surface of ND, (110) surface of Cu, and (100) surface of Zn, were selected for comparison. The ND (110) surface displayed a significant decrease of 0.54 eV in work function, corroborating a stronger interaction with the adsorbed Zn. In contrast, the Zn (100) and Cu (110) surfaces showed smaller changes in work function, further confirming the preferred adsorptions of Zn on ND surfaces. The variations of electron density for Zn adsorption on different surfaces of ND, Zn, and Cu were presented in Figure 1i and Figure S5, Supporting Information, where the yellow and blue isosurfaces represented the electron depletion and accumulation, respectively. It was revealed that the stronger adsorption of Zn on ND was correlated with a higher level of charge transfer between Zn and the ND surface.

The morphologies of Zn anodes with and without a ND layer after Zn stripping and deposition were characterized to investigate the influences of ND coating on Zn deposition behavior. After Zn plating for 1 h at a current density of 5 mA cm⁻², irregular dendrites were observed on the pristine zinc anode (**Figure 2a,b**). Correspondingly, homogeneous Zn plating without Zn dendrites was achieved under the ND protection layer at the same current density of 5 mA cm⁻² (Figure 2c,d). The morphologies of Zn an-

odes after plating at various current densities of 1 and 10 mA cm⁻² were also investigated, where the bare Zn anode exhibited a rough surface with numerous dendrites and plaques (Figure S6, Supporting Information) and the Zn-ND anode maintained an even and uniform surface structure (Figure S7, Supporting Information) under the same current density. Figure S8, Supporting Information showed the upper surface morphology of ND coatings after cycling in symmetric cells. The deposition behavior under various current densities and plating times were explored. It was found that Zn did not appear on the upper surface of coating under low current density of 1 mA cm⁻² and capacity of 1mAh cm⁻² and 5mAh cm⁻² (Figure S8a,b, Supporting Information). When the current density was further increased to 10 mA cm⁻², the upper surface of ND layer still showed no obvious Zn plating after plated for 1 and 2 h (Figure S8c,d, Supporting Information), indicating the insulating nature of ND coating. Figure 2e showed the hydrophilicity comparison between the pristine Zn anode and Zn-ND anode. The static water contact angle of the pristine Zn anode was measured as 93.4°, whereas it reduced to 53° when the ND layer was applied. This result indicated that the ND coating was more hydrophilic which facilitated electrolyte permeation and diffusion, thus promoting a more uniform Zn^{2+} flux at the interface between the ND layer and Zn anode.[17c]

The Zn deposition behavior was studied using the chronoamperometry method under a constant overpotential of −150 mV, in which the variation of current density with time reflected the nucleation behavior and the microscopic change of the Zn anode surface. As illustrated in Figure S9, Supporting Information, the plating current density of bare Zn electrode continuously increased beyond 30 mA cm⁻² after 40 s, indicating an irregular and random 2D diffusion process with uncontrolled deposition behavior. The absorbed Zn^{2+} diffused laterally and accumulated vertically on the anode surface, leading to the formation of Zn dendrites.[19] In contrast, the Zn foil with an ND top layer showed fast initial Zn nucleation and 2D diffusion within 5 s, followed by a steady 3D diffusion with a smaller current density of 22 mA cm⁻². This indicated the constrained lateral diffusion of Zn^{2+}, which was associated with uniform nucleation and stable Zn plating.[20] The formation of dendrites strongly depended on the ionic and electric field distribution at interfacial area between the anode and electrolyte.

To gain further insights into the Zn deposition on various surfaces, the corresponding diffusion energy barriers were compared to demonstrate the potential behavior of Zn deposit based on two different diffusion pathways, that is, top-to-top and hollow-to-hollow. For the top-to-top pathway, the (110), (111), and (100) of ND surfaces exhibited diffusion barriers of 0.15, 0.22, and 0.31 eV, respectively (Figure 2f, Figure S10a–c, Supporting Information), whereas the (100), (101), and (002) of Zn substrate were 0.59, 0.70, and 0.55 eV, respectively (Figure 2g, Figure S10d–f, Supporting Information). Considering Zn atoms had a higher tendency to be adsorbed on the (002) surface as compared to other Zn surfaces, Zn diffusion on ND surfaces was overall easier than that on Zn surfaces. The diffusion of Zn became even more difficult on the Cu surfaces, where the smallest diffusion barrier was 0.57 eV on the (111) surface (Figure 2h, Figure S10g–i, Supporting Information). Similarly, for the hollow-to-hollow diffusion pathway, although the diffusion energy barriers of Zn^{2+} on ND, Zn, and Cu changed compared
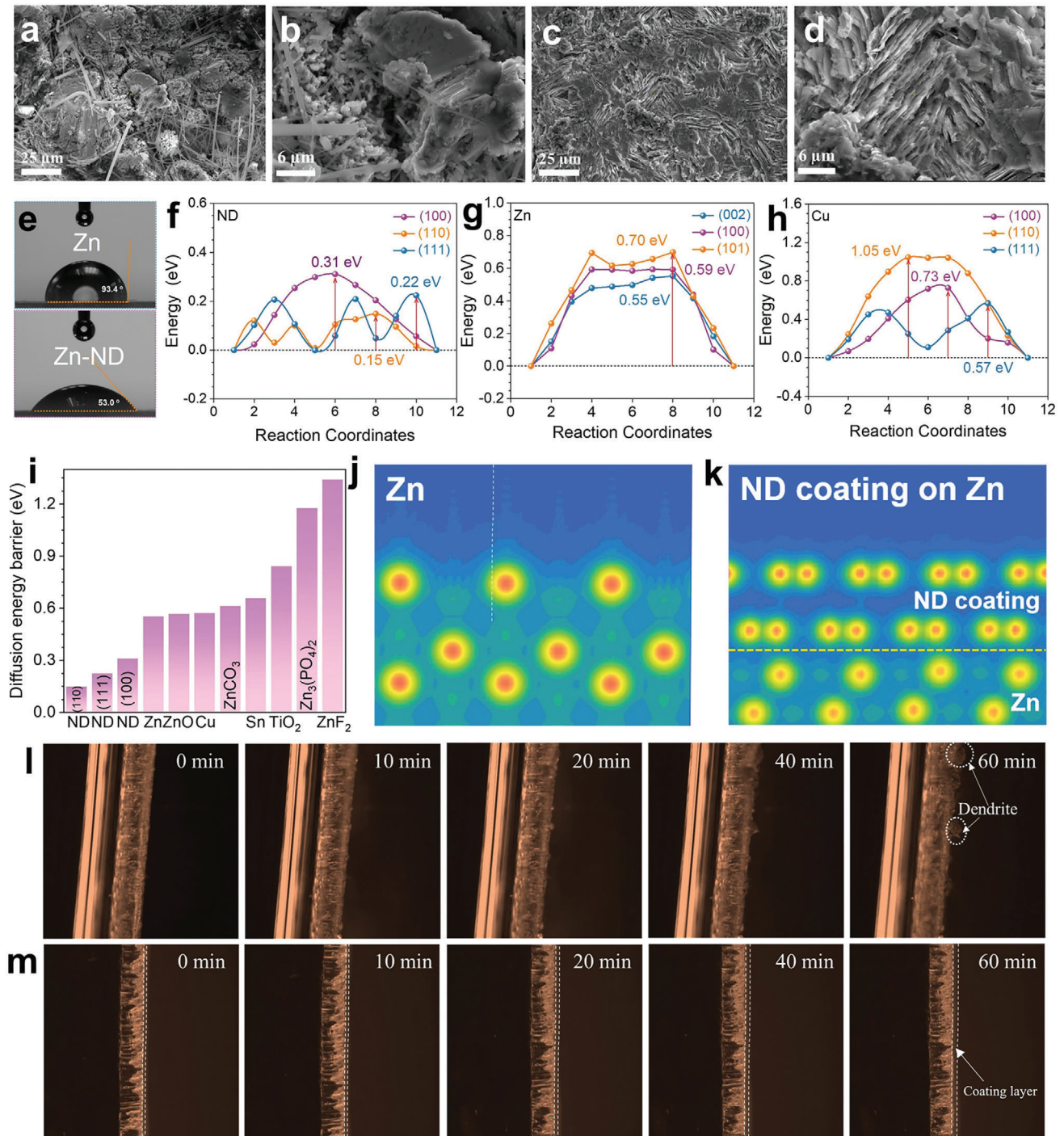
ADVANCED
SCIENCE NEWS

www.advancedsciencenews.com

ADVANCED
ENERGY
MATERIALS

www.advenergymat.de

Figure 2. SEM images of Zn deposition on a,b) pristine Zn foil, and c,d) under ND protection layer after plating and stripping at 5 mA cm^{-2} for 1 h, ND layer was removed by DMF solution. e) In situ contact angle tests for pristine Zn and Zn-ND anodes. The energy barriers for Zn migrations on the surfaces of f) ND, g) Zn, and h) Cu based on the top-to-top diffusion pathway. i) The lowest energy barrier comparison for Zn migrations on the surfaces of different materials with ND based on the top-to-top diffusion pathway. Simulated local electrostatic potential distributions on the surfaces of j) pristine Zn and k) ND-coated Zn surfaces. In situ optical microscopy characterization of the Zn plating processes l) on the Zn electrode and m) at the interface between ND layer and Zn in home-made transparent cells at 5 mA cm^{-2} for 60 min.

ADVANCED
SCIENCE NEWS

www.advancedsciencenews.com

ADVANCED
ENERGY
MATERIALS

www.advenergymat.de

with top-to-top diffusion pathway, the diffusion energy barriers on ND surface showed an overall lower value than those on Zn and Cu surface (Figures S11 and S12, Supporting Information). Owing to the larger diffusion barrier, the uneven aggregations of Zn became more likely to occur on both Zn and Cu electrode surfaces. However, the adsorbed Zn^{2+} ions onto the ND surface had a smoother diffusion path and uniform distribution, eventually suppressing dendrite formation.[15,21] The diffusion energy barriers of Zn on the ND surfaces, Zn and Cu surface with lowest value, and other reported artificial coatings or solid electrolyte interfaces (SEI) for Zn anode protection, including ZnO,[22] Sn,[23] $ZnCO_3$,[24] $Zn_3(PO_4)_2$,[25] TiO_2,[26] and ZnF_2,[27] were compared in Figure 2i and Figure S13, Supporting Information. It was evident that ND showed considerably lower overall energy barriers among all these materials, demonstrating its significant role in achieving the dendrite-free Zn anode.

In addition, it has been well accepted that the distribution of surface potential on the electrode surfaces play a crucial role in determining the electric field, which in turn, affects the Zn deposition. As depicted in the simulation result (Figure 2j), the pristine Zn surface exhibited an uneven potential distribution, which resulted in the accumulations of electrons near the regions with maximum electric field strength. Due to the self-accelerating tip effect,[28] the initially formed protuberances gradually developed into irregular and sharp dendrites and bulk deposits, eventually leading to battery failure. However, the introduction of ND on the electrode surface promoted a more uniform potential distribution due to the size effect, which enabled a more uniform flux distribution of Zn ions over the surface (Figure 2k). Consequently, protuberances were efficiently eliminated during the early stage of nucleation, so the flat Zn deposition was achieved. These theoretical calculations and simulations unraveled that the surface coating of diamond significantly promoted the Zn adsorption and diffusion, as well as the uniformity of electrical field distribution, which were key factors in suppressing dendrite formation and achieving smooth Zn deposition. In situ optical microscopy observations further verified that the bare Zn surface formed small Zn protrusions within 10 min, which grew larger and developed noticeable dendrite after 1 h (Figure 2l). In contrast, the ND coating effectively suppressed dendrite formation under the same deposition conditions, resulting in uniform zinc plating. (Figure 2m).

The stability and electrochemical performance of symmetric cells assembled with pristine Zn electrodes and Zn-ND electrodes were evaluated comparatively through long-term cycling experiments. **Figure 3a** illustrated the cycling lifespan and stability of the symmetric Zn-ND battery, which demonstrated over 3600 h (with a total cumulative capacity over 3.6 Ah cm^{-2}) of operation and a small voltage hysteresis of only 22 mV at a current of 1 mA cm^{-2} and a capacity of 1 mA h cm^{-2}. In contrast, the cell with pristine Zn||Zn electrodes broke down after only 260 h (0.26 Ah cm^{-2}) and exhibited a large voltage hysteresis of 50 mV. The Zn-ND electrodes also showed good cycling stability at higher current densities of 3 and 10 mA cm^{-2}, with capacities of 3 and 5 mAh cm^{-2}, respectively. As shown in Figure 3b, the Zn-ND||Zn-ND symmetric cell maintained stable cycling performance for over 2250 h at a high current density of 3 mA cm^{-2} and a capacity of 3mAh cm^{-2}, and the total cumulative capacity also reach up to 6.75 Ah cm^{-2}, outperforming the pris-

tine Zn electrodes. The voltage hysteresis of Zn-ND anode was also as small as only 28 mV. Furthermore, the Zn-ND symmetric cell continued to operate stably for over 1000 h at an even higher current density of 10 mA cm^{-2} and a higher capacity of 5 mAh cm^{-2} with total cumulative capacity of 10.16 Ah cm^{-2} (Figure 3c). The cycling performance of this symmetric cell surpassed most previously reported Zn anode protection strategies (Table S1, Supporting Information), demonstrating the advantages of the ND coating for zinc anode protection. Besides, it also showed that a larger cumulative capacity can be acquired with increase of current density. Figure 3d also demonstrated that the Zn-ND electrodes delivered better rate performance and smaller voltage hysteresis compared to the pristine Zn electrodes as the current density increased from 1, 3, 5 to 10 mA cm^{-2}, and then decreased to 1 mA cm^{-2}. It was shown that the voltage hysteresis became smaller after the current density decreased to 1 mA cm^{-2}, because more nucleation sites were formed on Zn-ND surface, and the surface area also became larger after cycling under 10 mA cm^{-2}. As a result, the interface resistance became lower, which contributed to a smaller voltage hysteresis. Notably, the voltage hysteresis of the symmetric cell was smaller than those of most previously reported results (Figure 3e).[5a,8c,24,29] This low voltage hysteresis can be attributed to favorable nucleation process and faster de-solvation kinetics associated with the ND coating.[23b,30]

A Cu||Zn asymmetric cell was assembled to analyze the Columbic efficiency (CE) of Zn^{2+} stripping/plating. The nucleation overpotential of Zn^{2+} on Cu-ND electrode was significantly smaller than that on the pristine Cu electrode (Figure 3f and Figure S14, Supporting Information), indicating a pronounced reduction in the Zn nucleation barrier provided by the ND coating. The Cu-ND electrode displayed an average CE of 99.5% over 1100 cycles with a high total cumulative capacity of 2.2 Ah cm^{-2} under 1 mA cm^{-2} (Figure 3g). In contrast, Zn plating on pristine Cu electrode exhibited inferior cycling performance of less than 100 cycles (0.11 Ah cm^{-2}). The cycling performance of the Cu-ND||Zn cell in this work exceeded those of most reported results at the same current density of 1 mA cm^{-2} and capacity of 1 mAh cm^{-2}, (Figure S15, Supporting Information). The excellent electrochemical performance for Cu-ND||Zn cells was attributed to the smooth and reversible Zn plating at the interface between Cu electrode and ND layer, which was confirmed by the Zn plating morphology. In the case of Cu||Zn cells, after plating for 1 h, random and large zinc clusters with sizes between 20 and 50 μm grew loosely on the Cu surface at current densities ranging from 0.25 to 3 mA cm^{-2} (Figure 3h and Figure S16, Supporting Information). The side-view of SEM and the corresponding elemental mapping images of Zn plating on the Cu electrode confirmed the poor deposition behavior of Zn (Figure 3i), and the confocal laser scanning microscopy (CLSM) revealed obvious humps and large altitude variation (−20 to 28.7 μm) due to the growth of Zn dendrites and by-products on the pristine Cu electrode (Figure 3j). In comparison, the Zn deposition at the interface between Cu electrode and ND layer exhibited a uniform and smooth surface without dendrite formation at current densities of 0.25, 1 and 3 mA cm^{-2}, respectively for 1 h (Figure 3k and Figure S17, Supporting Information), while the cross-sectional SEM and EDX mapping images of Zn on modified Cu electrode verified the deposition of Zn with an even thickness (Figure 3l). Moreover,
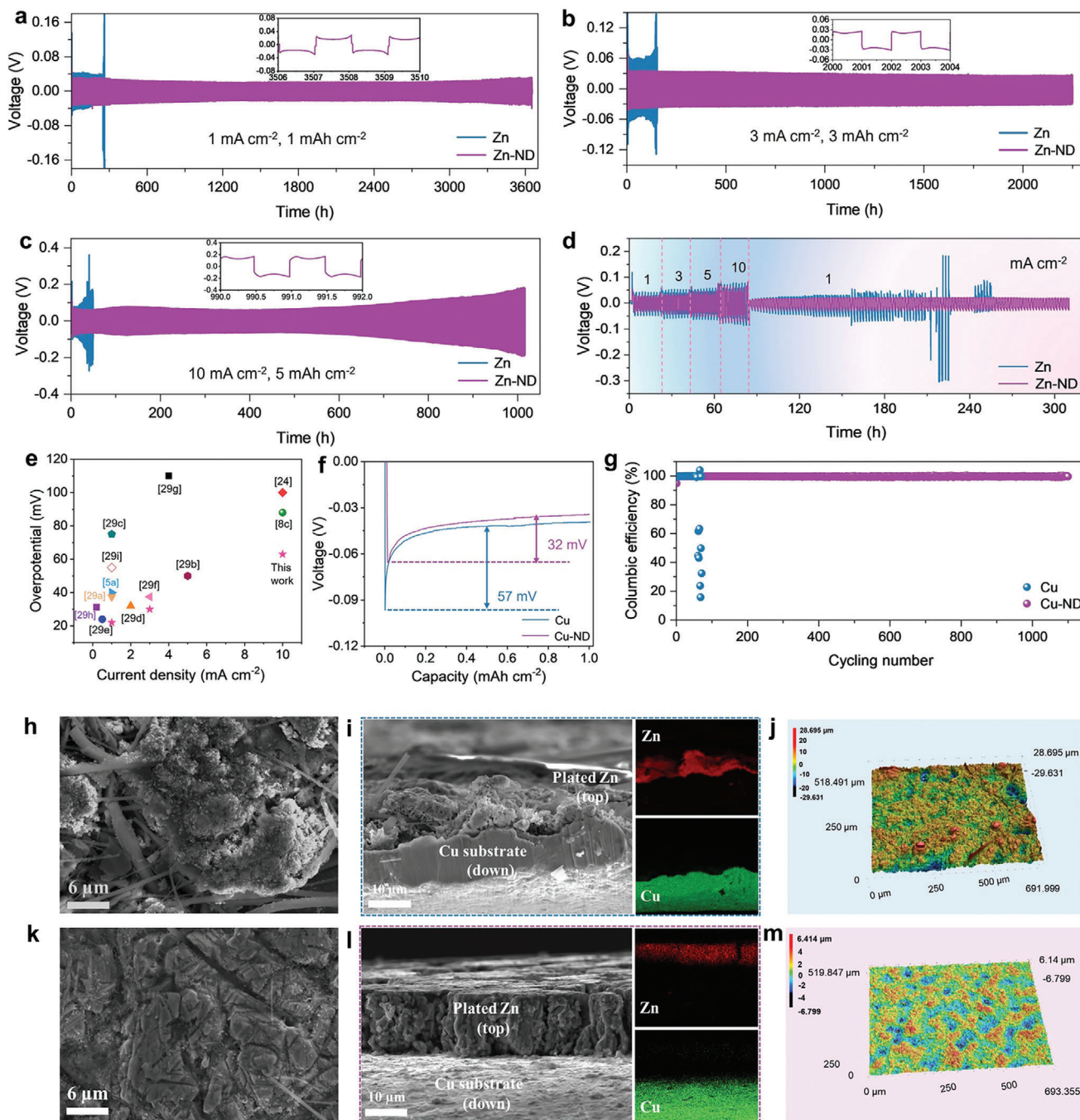
**ADVANCED
SCIENCE NEWS**

www.advancedsciencenews.com

**ADVANCED
ENERGY
MATERIALS**

www.advenergymat.de

Figure 3. Cycling stability of the Zn||Zn and Zn-ND||Zn-ND symmetric cells at a) current density of 1 mA cm^{-2} and area capacity of 1 mAh cm^{-2}, b) current density of 3 mA cm^{-2} and area capacity of 3 mAh cm^{-2}, and c) current density of 10 mA cm^{-2} and area capacity of 5 mAh cm^{-2}. d) Rate performance of assembled symmetric cells. e) A comparison of voltage hysteresis of Zn deposition between this work and reported literature. f) Voltage-capacity curves measured at 1 mA cm^{-2} for Cu||Zn and Cu-ND||Zn half cells. g) CEs of the asymmetric cells at 1 mA cm^{-2} and 1 mAh cm^{-2}. h) SEM image of Zn plating at 3 mA cm^{-2} for 1 h on Cu foil. i) Side-view SEM and EDX mapping images of zinc deposition on Cu foil. j) CLSM image of zinc deposition on Cu foil at current density of 5 mA cm^{-2} for 1 h. k) SEM image of Zn plating at 3 mA cm^{-2} for 1 h at the interface between Cu electrode and ND coating, ND layer was removed by DMF solution. l) Side-view SEM and EDX mapping images of zinc deposition at the interface between Cu electrode and ND coating, ND layer was removed by DMF solution. m) CLSM image of zinc deposition at the interface between Cu electrode and ND coating at current density of 5 mA cm^{-2} for 1 h where ND layer was removed.
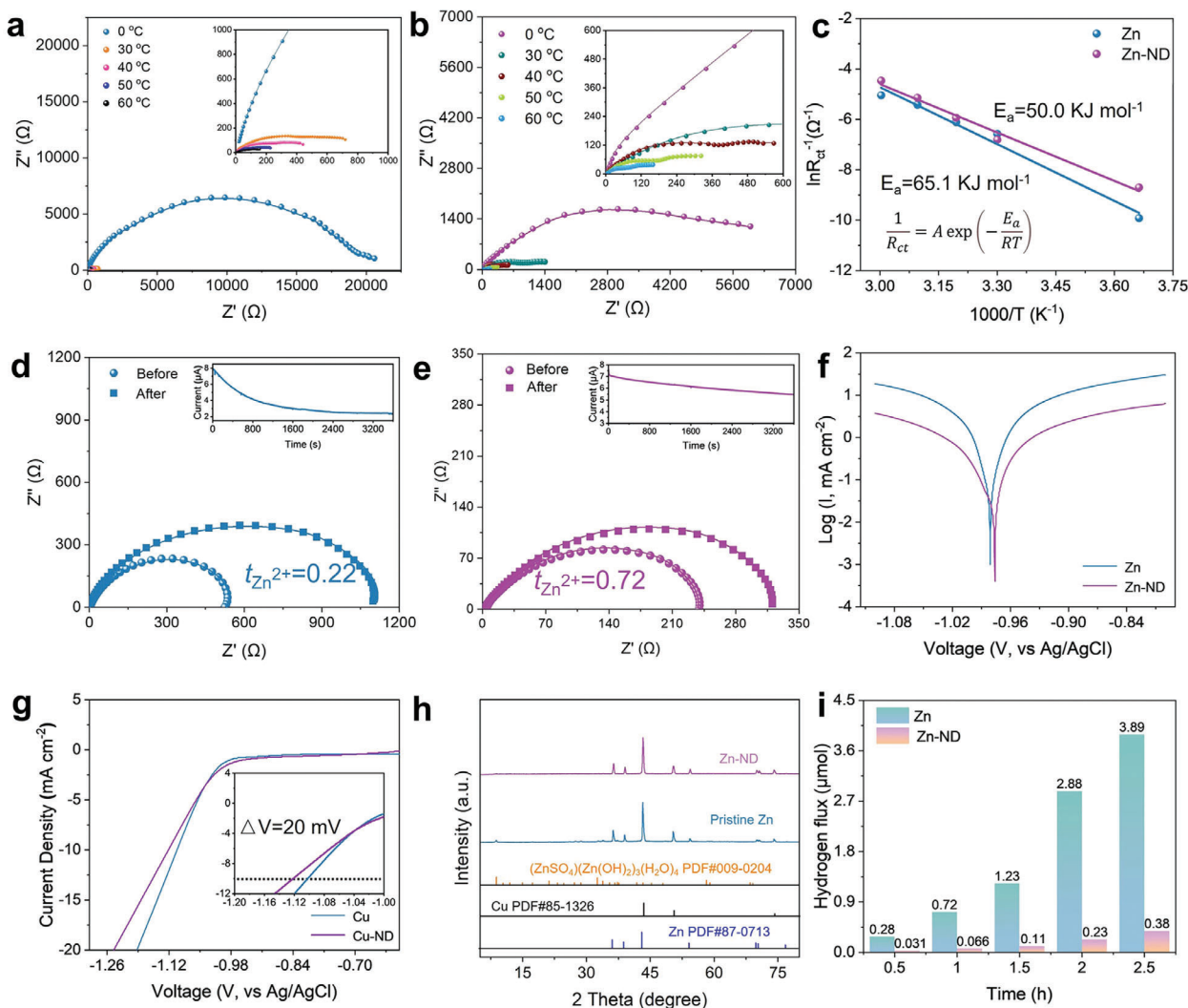
**ADVANCED
SCIENCE NEWS**

www.advancedsciencenews.com

**ADVANCED
ENERGY
MATERIALS**

www.advenergymat.de

Figure 4. Reaction Kinetics and anti-corrosion performance of Zn and Zn-ND Anodes. Temperature-dependent electrochemical impedance spectroscopy (EIS) results of symmetric cells assembled with a) bare Zn and b) Zn-ND electrodes. c) The Arrhenius curves and corresponding activation energies obtained for bare Zn and Zn-ND electrode. Nyquist plots of d) the bare Zn and e) the Zn-ND electrodes before and after chronoamperometry (CA) measurements, along with the calculated Zn^{2+} transference number. f) Linear polarization curves of Zn and Zn-ND anodes obtained using a three-electrode system. g) Electrochemical stability windows for hydrogen evolution, measured by linear sweep voltammetry at 1 mV s^{-1} in a three-electrode system. h) XRD patterns of the bare Zn and Zn-ND anodes after 10 cycles at 1 mA cm^{-2}. i) Hydrogen evolution flux over time at 5 mA cm^{-2}, with a fixed electrode area of 1 cm^{-2} and an electrolyte volume of 25 mL.

laser microscopy indicated that dense and homogeneous Zn was deposited at the interface between ND layer and Cu substrate with an even surface and a much-reduced altitude variation of ≈4.2 µm (Figure 3m). The optical photographs in Figure S18, Supporting Information showed the denser Zn deposited with more even morphology at the interface between Cu electrode and ND coating compared to that on the pristine Cu electrode where many areas were not covered by deposited Zn.

The de-solvation energy barriers for Zn^{2+} were determined by measuring the resistance of symmetric batteries over a temperature range of 0 to 60 °C (**Figure 4a,b**), the equivalent circuit was illustrated in Figure S19, Supporting Information. As depicted in Figure 4c, the Zn-ND anode presented a lower activation energy of 50.0 kJ mol^{-1} than that of bare Zn (65.1 kJ mol^{-1}) accord-

ing to the Arrhenius equation inserted in Figure 4c. The lower de-solvation barrier of the Zn-ND anode implied the enhanced de-solvent sheath ability and improved transmission kinetics of Zn^{2+} ions.[31] The Zn^{2+} transfer number can identify the transport efficiency of Zn^{2+} and the suppression of anion movement in the electrolyte, which played a crucial role in maintaining a uniform electrolyte concentration gradient and inhibiting side reactions at the anode.[32] In this study, the transfer number was estimated using the chronoamperometry (CA) method with a potentiostatic polarization of 10 mV, according to Equation (1):

$$t+ = \frac{I_s(\nabla V - I_0 R_0)}{I_0(\nabla V - I_s R_s)} \quad (1)$$

ADVANCED
SCIENCE NEWS

www.advancedsciencenews.com

ADVANCED
ENERGY
MATERIALS

www.advenergymat.de

where ∇V is the applied polarization potential, I_0 and I_s are the initial and steady-state current, respectively, and Ro and Rs are resistances of Zn‖Zn symmetric battery before and after polarization, respectively. As shown in Figure 4d,e and Figure S20, Supporting Information, the bare zinc anode displayed a low $t_{Zn^{2+}}$ of 0.22, which was attributed to the strong solvation effect of Zn^{2+} ions and H_2O or SO_4^{2-} anions.[33] The low $t_{Zn^{2+}}$ can lead to a large concentration gradient of Zn ion between the anode and the electrolyte, resulting in limited electrochemical performance at high charge–discharge rates.[34] On the other hand, the Zn^{2+} transport number measured with Zn-ND anode increased to 0.72, which was significantly higher than that of pure Zn anode. The enhanced Zn ion transfer number was attributed to the strong interaction between ND coating and H_2O/SO_4^{2-} anions, as well as the easier Zn^{2+} diffusion process.

The anti-corrosion effect of ND coating was evaluated through linear polarization measurements and quantitative analysis of hydrogen evolution by ex situ gas chromatography test. The Zn-ND anode showed a lower corrosion current density (i_{corr}) compared to the pristine zinc anode (Figure 4f). The reduced i_{corr} indicated superior anti-corrosion performance and lower corrosion reaction kinetics. Meanwhile, HER on the anode was also suppressed (Figure 4g) with a 20 mV negative shift in overpotential at the current density of 10 mA cm^{-2}. An intersection point appeared in the enlarged curves, indicating that both electrodes exhibited the same current density for the reduction reaction at the potential of -1.041 V. When the applied potential further increased, the reduction reaction rate on Cu-ND became slower than on Cu. This result reflected the inhibition effect of ND coating on HER. XRD analysis of Zn electrode after cycling for 10 cycles at 1 mA cm^{-2} in a 2.0 M ZnSO$_4$ aqueous electrolyte was performed to investigate the occurrence of side reactions in a slightly acidic electrolyte. Several new peaks were observed for the pure Zn electrodes, which could be assigned to ZnSO$_4$·3 Zn (OH)$_2$·5H$_2$O (JCPDS No. 009–0204). In contrast, the Zn-ND anode remained almost unchanged under the same conditions (Figure 4h). Elemental mapping (Figure S21a, Supporting Information) of the pristine Zn anode after soaking for 5 days in the aqueous electrolyte revealed an obvious presence of S elements, indicating the formation of by-products. However, it was much weaker for Zn-ND anode (Figure S21b, Supporting Information), indicating a lower formation of by-products. A battery–gas chromatograph (GC) system was utilized to detect hydrogen generation by monitoring the evolved hydrogen flux during the Zn charging–discharging process in a 2 M ZnSO$_4$ aqueous electrolyte at 5 mA cm^{-2}, with a fixed anode area of 1 cm^{-2}, electrolyte volume of 25 mL, and electrolytic tank volume of 100 mL. As shown in Figure 4i, the quantity of generated hydrogen flux operated by the symmetric Zn‖Zn cell was 0.28 µmol after 0.5 h, and increased to 3.89 µmol after 2.5 h. In comparison, the hydrogen evolution quantity from the Zn-ND anode was only 10% of that from the pristine zinc anode.

Aqueous full cells, consisting of a MnO$_2$ cathode, a Zn anode (or a Zn-ND anode), and a glass fiber (GF) separator, were assembled to assess the feasibility of the designed Zn-ND anode. The MnO$_2$ cathode, prepared by hydrothermal method, was characterized using XRD (Figure S22, Supporting Information). The diffraction peaks confirmed that the cathode consisted of pure δ-phase MnO$_2$ with layered structure and birnessite frame-

work (JCPDS: 80–1098). SEM images (Figure S23, Supporting Information) revealed the hexagonal nanoplates structure of the prepared cathode sample. Cyclic voltammetry (CV) measurements were conducted on the full battery (**Figure 5**a), and both curves exhibited similar shapes. The two pairs of redox peaks were assigned to the stepwise conversion of Mn^{4+}/Mn^{3+} and Mn^{3+}/Mn^{2+}. CV measurements were performed at various scan rates from 0.1 and 0.8 mV s^{-1} to further investigate the electrochemical reaction kinetics of full cells. The relation between peak current (i) and scan rates (v) follows Equations (2) and (3):

$$i(v) = av^b \tag{2}$$

$$\log(i) = \log(a) + b * \log(v) \tag{3}$$

where the slope part (b value) indicates the type of electrochemical reaction. The b value approaching 0.5 suggests that the electrochemical reaction is controlled by ionic diffusion, while the b value close to 1 implies the predominance of surface pseudocapacitance reaction during the electrochemical process.[35] The calculated results of b values in Figure S24, Supporting Information, indicated that the electrochemical reactions of the Zn‖MnO$_2$ battery were simultaneously controlled by ionic diffusion and pseudocapacitance. Furthermore, the b values of the Zn-ND anode were higher than those of the pristine electrodes, signifying faster reaction kinetics of the Zn-ND‖MnO$_2$ cell.[36]

The rate performance of the designed aqueous batteries was evaluated in the current density range of 0.2 to 2.5 A g^{-1} with a voltage range from 0.9 to 1.85 V. As depicted in Figure 5b, the Zn-ND‖MnO$_2$ cell exhibited a comparable discharge capacity with Zn‖MnO$_2$ cell under various current densities. The corresponding charge-discharge curves at 0.2 A g^{-1} (Figure 5c) presented two voltage platforms consistent with the peak positions in the CV curves. Long-term cycling performance of the Zn‖MnO$_2$ cell (Figure 5d) showed the low-capacity retention of 50.3% after 3200 cycles. However, when equipped with the Zn-ND anode, the assembled full cell demonstrated a dramatically improved capacity retention ratio of nearly 100% after 2800 cycles and 90% after 3500 cycles at 2 A g^{-1}. Moreover, the surface morphology of the Zn anodes after long-term cycling at 2 A g^{-1} (Figure 5e) revealed uneven Zn deposition and mossy-like dendrites on the surface of the pristine Zn anode. In comparison, the full cell with the ND layer modified Zn anode exhibited a smoother and denser Zn deposition layer under ND coating after long-term cycling, confirming the stable plating/stripping of metallic Zn induced by the ND coating. Besides, the cross-sectional SEM image of Zn-ND anode disassembled from the cycled full cell was shown in Figure S25, Supporting Information, it is found that ND coating firmly adhered on surface of Zn anode, indicating excellent stability of this multifunctional ND layer.

Zinc ion hybrid supercapacitors (ZHSCs) employing activated carbon cathode were also assembled to evaluate the stability of the Zn-ND anode. The electrochemical performance of the ZHSCs was investigated using CV and the galvanostatic charge–discharge (GCD) techniques within a voltage window of 0–1.9 V. As shown in Figure S26a,b, Supporting Information, all the curves exhibited a quasi-rectangular shape with minor distortion as the scan rate increased from 10 to 200 mV s^{-1}, indicating
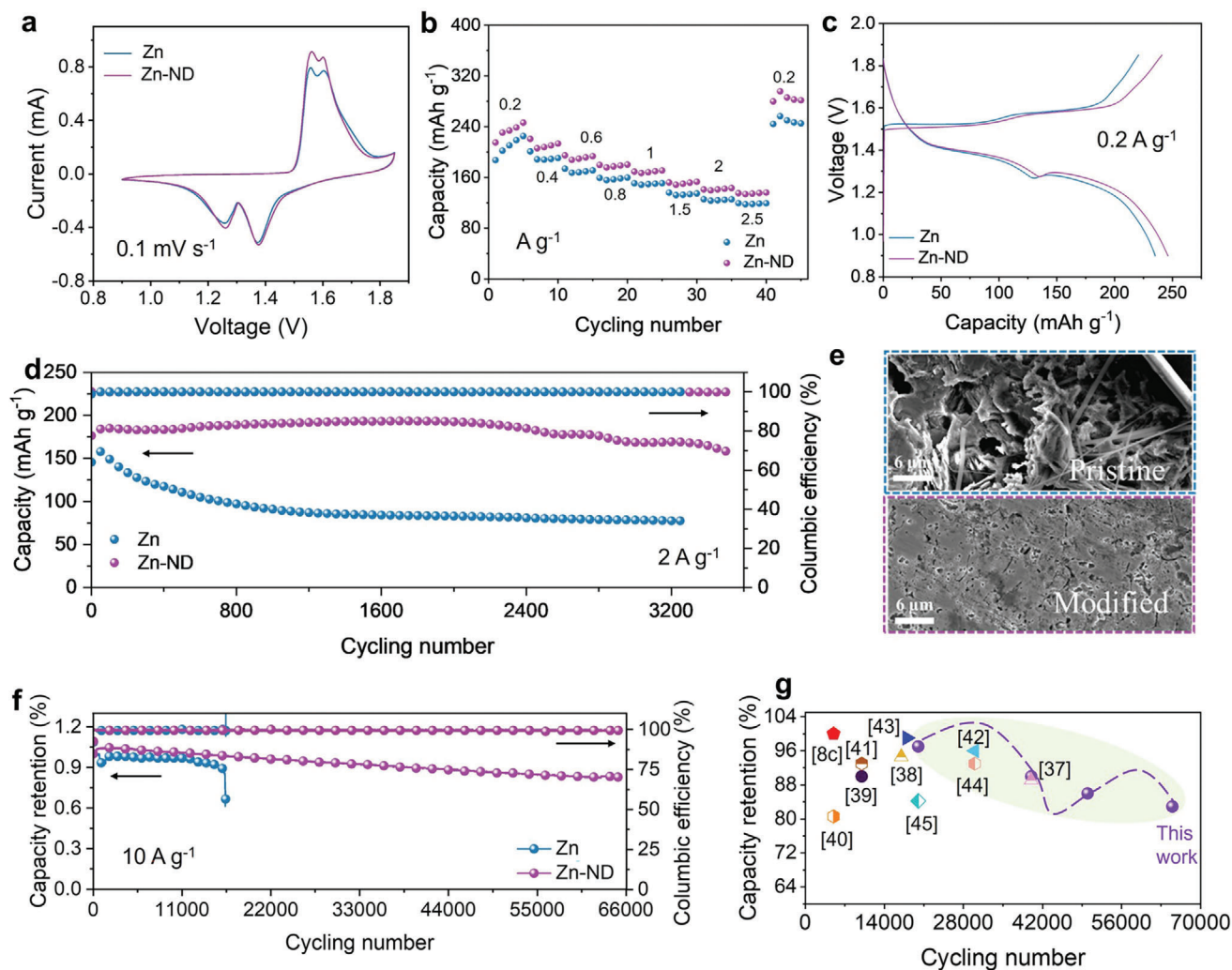
Figure 5. Electrochemical performance of full cells, and zinc ion hybrid capacitors assembled with Zn and Zn-ND anodes. a) CV curves of the full cells at a rate of 0.1 mV s^{-1} using the pristine Zn anode and the Zn-ND anode. b) Rate performance of the full cells at varied rates from 0.2 to 2.5 A g^{-1}. c) Galvanostatic charge-discharge curves at 0.2 A g^{-1}. d) Long-term cycling performance and corresponding Coulombic efficiencies obtained at the current of 2 A g^{-1}. e) SEM surface morphology images of pristine and modified zinc anode disassembled from the cycled full cells; ND layer was removed with DMF. f) Long-term cycling performance of the capacitors at the current density of 10 A g^{-1}. g) Comparison of the cycling number and capacity retention of the zinc ion hybrid capacitors reported in this work and literature.

the behavior of quasi-ideal electrochemical double-layer capacitors (EDLC). From the GCD curves of the ZHSCs at various current densities ranging from 0.2 to 20 A g^{-1} (Figure S26c–e, Supporting Information), specific capacitances of 171.2 mAh g^{-1} at 0.2 A g^{-1} and 60.2 mAh g^{-1} at 20 A g^{-1} were obtained. Notably, the devices delivered an initial increase in specific capacity, likely due to the activation process of the cathode, and the long-term cycling at a current density of 10 A g^{-1} revealed a significant difference in specific capacity (Figure 5f). The capacity of the ZHSCs with the pristine Zn anode decayed dramatically after running for about 15, 000 cycles, indicating the onset of device degradation. The poor cycling performance of the ZHSCs with the pristine Zn anode can be attributed to the growth of dendrites and the formation of by-products at the electrode-electrolyte interface. In contrast, the ZHSCs with Zn-ND anode operated stably

for ≈65 000 cycles while maintaining 83.0% of its initial capacity. The cycling performance of the ZHSCs with Zn-ND anode and carbon cathode surpassed many typical zinc ion hybrid capacitors (Figure 5g), such as Zn||poly-(sodium dodecyl sulfate-stearyl methacrylate-acrylamide)-Zn(OTf)$_2$||N-doped porous carbon,[37] Zn||P(AM-*co*-SBMA) hydrogel electrolyte||activated carbon (AC) Zn-ion hybrid micro-supercapacitor,[38] Zn||zinc(II) betaine complex||AC capacitors,[39] Zn||AC zinc ion hybrid capacitors,[8c] Zn||ZnSO$_4$–7H$_2$O–3 dimethylformamide (DMF)||AC,[40] Coaxial fiber-shaped Zn-ion hybrid supercapacitors (CFZHSCs),[41] Zn||ZnSO$_4$-sodium carboxymethyl cellulose (CMC-Na)||AC,[42] Zn||ZnSO$_4$ with CMC-Na binder additive||AC,[43] Zn||ZnSO$_4$ -DMF additive||AC,[44] Zn||Zn(TFSI)$_2$-dimethylsulfoxide additive||AC,[45] highlighting the excellent protective ability of the ND coatings on the Zn anodes.

3. Conclusion

A novel ND coating was designed and implemented for the dendrite-free Zn anodes with high stability and reversible zinc deposition behavior. The effectiveness of the ND layer was supported by both theoretical calculations and experimental results. The ND coating, characterized with high surface energy, rich nucleation sites (in the order of 10^{12} cm^{-2}), and low zinc ion diffusion energy barrier, facilitated the preferential adsorption of Zn ions and promoted uniform ion flux, resulting in even and dense Zn deposition without dendrite growth. As a result, Zn-ND anodes exhibited a significantly prolonged lifespan, demonstrating steady operation in symmetric cells for over 3600 h at 1 mA cm^{-2} and 1100 h at 10 mA cm^{-2}, respectively. Furthermore, the Zn||Cu-ND half-cell displayed exceptional long cycling performance with 1100 cycles at 1 mA cm^{-2} and a high average CE of 99.5%. Moreover, the Zn-ND||MnO$_2$ full cell delivered remarkable cycling performance of 2800 cycles with 100% and 3500 cycles with 90% capacity retentions at 2 A g^{-1}, respectively. The cycling performance of hybrid capacitors prepared with Zn-ND and activated carbon electrodes was also greatly improved with a capacity retention of 83.0% after 65,000 cycles at 10 A g^{-1}. These finding highlighted the potential applications of ND protective coating as an effective strategy for suppressing dendrite formation and by-product accumulation in Zn anodes.

Supporting Information

Supporting Information is available from the Wiley Online Library or from the author.

Conflict of Interest

The authors declare no conflict of interest.

Data Availability Statement

The data that support the findings of this study are available from the corresponding author upon reasonable request.

[1] W. C. Du, E. H. X. Ang, Y. Yang, Y. F. Zhang, M. H. Ye, C. C. Li, *Energy Environ. Sci.* **2020**, *13*, 3330.

[2] H. Z. Ren, S. Li, B. Wang, Y. Y. Zhang, T. Wang, Q. Lv, X. Y. Zhang, L. Wang, X. Han, F. Jin, C. Y. Bao, P. F. Yan, N. Zhang, D. L. Wang, T. Cheng, H. K. Liu, S. X. Dou, *Adv. Mater.* **2023**, *35*, 2208237.

[3] a) X. B. Cheng, R. Zhang, C. Z. Zhao, Q. Zhang, *Chem. Rev.* **2017**, *117*, 10403; b) X. R. Chen, B. C. Zhao, C. Yan, Q. Zhang, *Adv. Mater.* **2021**, *33*, 2004128; c) Z. Z. Li, M. Q. Peng, X. L. Zhou, K. Shin, S. Tunmee, X. M. Zhang, C. D. Xie, H. Saitoh, Y. P. Zheng, Z. M. Zhou, Y. B. Tang, *Adv. Mater.* **2021**, *33*, 2100793.

[4] a) M. Zhou, S. Guo, J. L. Li, X. B. Luo, Z. X. Liu, T. S. Zhang, X. X. Cao, M. Q. Long, B. G. Lu, A. Q. Pan, G. Z. Fang, J. Zhou, S. Q. Liang, *Adv. Mater.* **2021**, *33*, 2100187; b) H. N. He, L. Zeng, D. Luo, J. He, X. L. Li, Z. P. Guo, C. H. Zhang, *Adv. Mater.* **2023**, *35*, 2211498.

[5] a) B. Y. Li, K. Yang, J. B. Ma, P. R. Shi, L. K. Chen, C. M. Chen, X. Hong, X. Cheng, M. C. Tang, Y. B. He, F. Y. Kang, *Angew. Chem., Int. Ed.* **2022**, *61*, 202212587; b) S. B. Wang, Q. Ran, R. Q. Yao, H. Shi, Z. Wen, M. Zhao, X. Y. Lang, Q. Jiang, *Nat. Commun.* **2020**, *11*, 1634.

[6] a) J. Zheng, G. Zhu, X. Liu, H. Xie, Y. Lin, Y. Zeng, Y. Zhang, A. N. Gandi, Z. Qi, Z. Wang, H. Liang, *ACS Energy Lett.* **2022**, *7*, 4443; b) Z. Bie, Q. Yang, X. Cai, Z. Chen, Z. Jiao, J. Zhu, Z. Li, J. Liu, W. Song, C. Zhi, *Adv. Energy Mater.* **2022**, *12*, 2202683; c) J. Zhou, M. Xie, F. Wu, Y. Mei, Y. Hao, R. Huang, G. Wei, A. Liu, L. Li, R. Chen, *Adv. Mater.* **2021**, *33*, 2101649; d) T. Wang, P. Wang, L. Pan, Z. He, L. Dai, L. Wang, S. Liu, S. C. Jun, B. Lu, S. Liang, J. Zhou, *Adv. Energy Mater.* **2023**, *13*, 2203523; e) X. S. Xie, S. Q. Liang, J. W. Gao, S. Guo, J. B. Guo, C. Wang, G. Y. Xu, X. W. Wu, G. Chen, J. Zhou, *Energy Environ. Sci.* **2020**, *13*, 503.

[7] a) M. M. Wang, J. L. Ma, Y. H. Meng, J. F. Sun, Y. Yuan, M. Chuai, N. Chen, Y. Xu, X. H. Zheng, Z. Y. Li, W. Chen, *Angew. Chem., Int. Ed.* **2022**, *62*, e202214966; b) F. W. Ming, Y. P. Zhu, G. Huang, A. H. Emwas, H. F. Liang, Y. Cui, H. N. Alshareef, *J. Am. Chem. Soc.* **2022**, *144*, 7160; c) M. Yang, J. C. Zhu, S. S. Bi, R. Wang, Z. Q. Niu, *Adv. Mater.* **2022**, *34*, 2201744.

[8] a) Y. Zong, H. He, Y. Wang, M. Wu, X. Ren, Z. Bai, N. Wang, X. Ning, S. X. Dou, *Adv. Energy Mater.* **2023**, *13*, 2300403; b) Y. Fang, X. S. Xie, B. Y. Zhang, Y. Z. Chai, B. A. Lu, M. K. Liu, J. Zhou, S. Q. Liang, *Adv. Funct. Mater.* **2022**, *32*, 2109671; c) Y. Li, X. Y. Peng, X. Li, H. Duan, S. Y. Xie, L. B. Dong, F. Y. Kang, *Adv. Mater.* **2023**, *35*, 2300019.

[9] H. N. Liu, J. G. Wang, W. Hua, H. H. Sun, Y. Huyan, S. Tian, Z. D. Hou, J. C. Yang, C. G. Wei, F. Y. Kang, *Adv. Sci.* **2021**, *8*, 2102612.

[10] a) X. M. Cai, W. Z. Tian, Z. K. Zhang, Y. Sun, L. Yang, H. C. Mu, C. Lian, H. B. Qiu, *Adv. Mater.* **2023**, *36*, 2307727; b) Y. Z. Wang, T. C. Guo, J. Yin, Z. N. Tian, Y. C. Ma, Z. X. Liu, Y. P. Zhu, H. N. Alshareef, *Adv. Mater.* **2022**, *34*, 2106937.

[11] a) J. H. Zhou, M. Xie, F. Wu, Y. Mei, Y. T. Hao, R. L. Huang, G. L. Wei, A. N. Liu, L. Li, R. J. Chen, *Adv. Mater.* **2021**, *33*, 2101649; b) K. Yun, G. H. An, *Chem. Eng. J.* **2024**, *479*, 147303.

[12] a) T. Wang, K. Yao, K. Li, J. S. Yu, *Energy Storage Mater.* **2023**, *62*, 102921; b) X. D. Zhu, X. Y. Li, M. L. K. Essandoh, J. Tan, Z. Y. Cao, X. Zhang, P. Dong, P. M. Ajayan, M. X. Ye, J. F. Shen, *Energy Storage Mater.* **2022**, *50*, 243.

[13] a) A. Jana, S. I. Woo, K. S. N. Vikrant, R. E. Garcia, *Energy Environ. Sci.* **2019**, *12*, 3595; b) Y. D. Liu, Q. Liu, L. Xin, Y. Z. Liu, F. Yang, E. A. Stach, J. Xie, *Nat. Energy* **2017**, *2*, 17083.

[14] a) S. F. Liu, X. Ji, J. Yue, S. Hou, P. F. Wang, C. Y. Cui, J. Chen, B. W. Shao, J. R. Li, F. D. Han, J. P. Tu, C. S. Wang, *J. Am. Chem. Soc.* **2020**, *142*, 2438; b) S. A. Abbas, H. A. Chen, A. Mohapatra, A. Singh, S. Li, C. W. Pao, C. W. Chu, *Small* **2022**, *18*, 2201349; c) D. Wang, W. Zhang, W. Zheng, X. Cui, T. Rojo, Q. Zhang, *Adv. Sci.* **2017**, *4*, 1600168.

[15] X. B. Cheng, M. Q. Zhao, C. Chen, A. Pentecost, K. Maleski, T. Mathis, X. Q. Zhang, Q. Zhang, J. J. Jiang, Y. Gogotsi, *Nat. Commun.* **2017**, *8*, 336.

[16] Y. Liu, Y.-K. Tzeng, D. Lin, A. Pei, H. Lu, N. A. Melosh, Z.-X. Shen, S. Chu, Y. Cui, *Joule* **2018**, *2*, 1595.

[17] a) H. Y. Huo, Y. Chen, J. Luo, X. F. Yang, X. X. Guo, X. L. Sun, *Adv. Energy Mater.* **2019**, *9*, 1804004; b) Z. Li, M. Peng, X. Zhou, K. Shin, S. Tunmee, X. Zhang, C. Xie, H. Saitoh, Y. Zheng, Z. Zhou, Y. Tang, *Adv. Mater.* **2021**, *33*, 2100793; c) S. H. Park, S. Y. Byeon, J. H. Park, C. Kim, *ACS Energy Lett.* **2021**, *6*, 3078.

[18] Y. Wang, T. Guo, J. Yin, Z. Tian, Y. Ma, Z. Liu, Y. Zhu, H. N. Alshareef, *Adv. Mater.* **2022**, *34*, 2106937.

[19] a) S. Zhou, Y. Wang, H. Lu, Y. Zhang, C. Fu, I. Usman, Z. Liu, M. Feng, G. Fang, X. Cao, S. Liang, A. Pan, *Adv. Funct. Mater.* **2021**, *31*, 2104361; b) X. Chen, W. Li, S. Hu, N. G. Akhmedov, D. Reed, X. Li, X. Liu, *Nano Energy* **2022**, *98*, 107269.

[20] W. L. Xie, K. Y. Zhu, H. M. Yang, W. S. Yang, *Adv. Mater.* **2024**, 2306154.

[21] R. Aogaki, T. Makino, *J. Electrochem. Soc.* **1984**, *131*, 46.

[22] Q. Ren, X. Tang, K. He, C. Zhang, W. Wang, Y. Guo, Z. Zhu, X. Xiao, S. Wang, J. Lu, Y. Yuan, *Adv. Funct. Mater.* **2023**, *34*, 2312220.

[23] a) Z. Y. Miao, M. Du, H. Z. Li, F. Zhang, H. C. Jiang, Y. H. Sang, Q. F. Li, H. Liu, S. H. Wang, *Ecomat* **2021**, *3*, 10; b) S. Y. Li, J. Fu, G. X. Miao, S. P. Wang, W. Y. Zhao, Z. C. Wu, Y. J. Zhang, X. W. Yang, *Adv. Mater.* **2021**, *33*, 2008424.

[24] Y. X. Zhu, H. Y. Hoh, S. S. Qian, C. Sun, Z. Z. Wu, Z. M. Huang, L. Wang, M. Batmunkh, C. Lai, S. Q. Zhang, Y. L. Zhong, *ACS Nano* **2022**, *16*, 14600.

[25] a) Y. Z. Chu, S. Zhang, S. Wu, Z. L. Hu, G. L. Cui, J. Y. Luo, *Energy Environ. Sci.* **2021**, *14*, 3609; b) S. Z. Zhang, M. H. Ye, Y. F. Zhang, Y. C. Tang, X. Q. Liu, C. C. Li, *Adv. Funct. Mater.* **2023**, *33*, 2208230.

[26] a) Q. Zhang, J. Y. Luan, X. B. Huang, Q. Wang, D. Sun, Y. G. Tang, X. B. Ji, H. Y. Wang, *Nat. Commun.* **2020**, *11*, 3961; b) Z. K. Guo, L. S. Fan, C. Y. Zhao, A. S. Chen, N. N. Liu, Y. Zhang, N. Q. Zhang, *Adv. Mater.* **2022**, *34*, 2105133.

[27] a) J. Han, H. Euchner, M. Kuenzel, S. M. Hosseini, A. Gross, A. Varzi, S. Passerini, *ACS Energy Lett.* **2021**, *6*, 3063; b) G. L. Wang, Q. Yao, J. J. Dong, W. J. Ge, N. A. Wang, Z. C. Bai, J. Yang, S. X. Dou, *Adv. Energy Mater.* **2024**, *14*, 2303221; c) T. T. Li, S. L. Hu, C. G. Wang, D. Wang, M. W. Xu, C. Y. Chang, X. J. Xu, C. P. Han, *Angew. Chem., Int. Ed.* **2023**, *62*, e202314883.

[28] a) D. M. Li, Y. Tang, S. Q. Liang, B. A. Lu, G. Chen, J. Zhou, *Energy Environ. Sci.* **2023**, *16*, 3381; b) L. Hong, X. M. Wu, Y. S. Liu, C. Y. Yu, Y. C. Liu, K. X. Sun, C. Y. Shen, W. Huang, Y. F. Zhou, J. S. Chen, K. X. Wang, *Adv. Funct. Mater.* **2023**, *33*, 2300952.

[29] a) J. B. Zhu, Z. Bie, X. X. Cai, Z. Y. Jiao, Z. T. Wang, J. C. Tao, W. X. Song, H. J. Fan, *Adv. Mater.* **2022**, *34*, 2207209; b) Y. W. Su, B. Z. Liu, Q. H. Zhang, J. Peng, C. H. Wei, S. Li, W. P. Li, Z. K. Xue, X. Z. Yang, J. Y. Sun, *Adv. Funct. Mater.* **2022**, *32*, 2204306; c) S. L. Liu, J. Vongsvivut, Y. Y. Wang, R. Z. Zhang, F. H. Yang, S. L. Zhang, K. Davey, J. F. Mao, Z. P. Guo, *Angew. Chem., Int. Ed.* **2023**, *135*, e202215600; d) S. W. Zhao, Y. J. Zhang, J. D. Li, L. M. Qi, Y. X. Tang, J. Zhu, J. Zhi, F. Q. Huang, *Adv. Mater.* **2023**, *35*, 2300195; e) H. Wang, Y. J. Chen, H. M. Yu, W. Liu, G. C. Kuang, L. Mei, Z. B. Wu, W. F. Wei, X. B. Ji, B. H. Qu, L. B. Chen, *Adv. Funct. Mater.* **2022**, *32*, 2205600; f) G. J. Liang, J. X. Zhu, B. X. Yan, Q. Li, A. Chen, Z. Chen, X. Q. Wang, B. Xiong, J. Fan, J. Xu, C. Y. Zhi, *Energy Environ. Sci.* **2022**, *15*, 1086; g) H. Zhang, S. Li, L. Q.

Xu, R. Momen, W. T. Deng, J. G. Hu, G. Q. Zou, H. S. Hou, X. B. Ji, *Adv. Energy Mater.* **2022**, *12*, 2200665; h) Y. Z. Wang, T. C. Guo, J. Yin, Z. N. Tian, Y. C. Ma, Z. X. Liu, Y. P. Zhu, H. N. Alshareef, *Adv. Mater.* **2022**, *34*, 2106937; i) L. Q. Zhang, J. J. Huang, H. L. Guo, L. F. Ge, Z. H. Tian, M. J. Zhang, J. T. Wang, G. J. He, T. X. Liu, J. Hofkens, D. J. L. Brett, F. L. Lai, *Adv. Energy Mater.* **2023**, *13*, 2203790.

[30] a) F. Bu, Y. Gao, W. B. Zhao, Q. H. Cao, Y. F. Deng, J. P. Chen, J. Pu, J. Y. Yang, Y. X. Wang, N. T. Yang, T. Meng, X. Y. Liu, C. Guan, *Angew. Chem., Int. Ed.* **2024**, *63*, e202318496; b) D. Xie, Z. W. Wang, Z. Y. Gu, W. Y. Diao, F. Y. Tao, C. Liu, H. Z. Sun, X. L. Wu, J. W. Wang, J. P. Zhang, *Adv. Funct. Mater.* **2022**, *32*, 2204066; c) Z. Xie, Y. Yuan, Z. Yao, M. Zhu, S. Y. Guo, P. Du, *Chem. Eng. J.* **2024**, *484*, 149601; d) J. Cao, D. D. Zhang, R. Chanajaree, Y. L. Yue, X. Y. Zhang, X. L. Yang, C. Cheng, S. Li, J. Q. Qin, J. Zhou, Z. Y. Zeng, *ACS Appl. Mater. Interfaces* **2023**, *15*, 45045.

[31] a) C. Ma, K. Yang, S. Zhao, Y. Xie, C. Liu, N. Chen, C. Wang, D. Wang, D. Zhang, Z. X. Shen, F. Du, *ACS Energy Lett.* **2023**, *8*, 1201; b) Y. P. Guo, P. Niu, Y. Y. Liu, Y. Ouyang, D. Li, T. Y. Zhai, H. Q. Li, Y. Cui, *Adv. Mater.* **2019**, *31*, 1900342; c) X. Wang, J. P. Meng, X. G. Lin, Y. D. Yang, S. Zhou, Y. P. Wang, A. Q. Pan, *Adv. Funct. Mater.* **2021**, *31*, 2106114.

[32] J. L. Schaefer, D. A. Yanga, L. A. Archer, *Chem. Mater.* **2013**, *25*, 834.

[33] J. Cao, D. D. Zhang, Y. L. Yue, R. Chanajaree, S. M. Wang, J. T. Han, X. Y. Zhang, J. Q. Qin, Y. H. Huang, *Nano Energy* **2022**, *93*, 106839.

[34] Q. P. Jian, T. S. Wang, J. Sun, B. Liu, T. S. Zhao, *Chem. Eng. J.* **2023**, *466*, 143189.

[35] V. Augustyn, J. Come, M. A. Lowe, J. W. Kim, P. L. Taberna, S. H. Tolbert, H. D. Abruña, P. Simon, B. Dunn, *Nature Mater.* **2013**, *12*, 518.

[36] a) X. Hu, Y. J. Liu, J. X. Chen, L. C. Yi, H. B. Zhan, Z. H. Wen, *Adv. Energy Mater.* **2019**, *9*, 1901533; b) R. Q. Dong, L. M. Zheng, Y. Bai, Q. Ni, Y. Li, F. Wu, H. X. Ren, C. Wu, *Adv. Mater.* **2021**, *33*, 2008810.

[37] G. Z. Guo, C. C. Ji, H. Y. Mi, C. Yang, M. J. Li, C. R. Sun, L. X. Sun, *Adv. Funct. Mater.* **2024**, *34*, 2308405.

[38] W. T. Zhang, F. J. Guo, H. Y. Mi, Z. S. Wu, C. C. Ji, C. C. Yang, J. S. Qiu, *Adv. Energy Mater.* **2022**, *12*, 2202219.

[39] P. Chen, X. H. Sun, T. Pietsch, B. Plietker, E. Brunner, M. Ruck, *Adv. Mater.* **2023**, *35*, 2207131.

[40] P. C. Zou, R. Q. Lin, T. P. Pollard, L. B. Yao, E. Y. Hu, R. Zhang, Y. B. He, C. Y. Wang, W. C. West, L. Ma, O. Borodin, K. Xu, X. Q. Yang, H. L. Xin, *Nano Lett.* **2022**, *22*, 7535.

[41] J. X. Zhao, Z. F. Cong, J. Hu, H. Y. Lu, L. T. Wang, H. B. Wang, O. I. Malyi, X. Pu, Y. N. Zhang, H. Y. Shao, Y. X. Tang, Z. L. Wang, *Nano Energy* **2022**, *93*, 106893.

[42] X. Fang, C. Hu, X. Y. Sun, H. Y. Wang, J. Li, *Adv. Energy Mater.* **2024**, *14*, 2302499.

[43] H. J. Huang, J. W. Yun, H. Feng, T. Tian, J. W. Xu, D. L. Li, X. Xia, Z. H. Yang, W. X. Zhang, *Energy Storage Mater.* **2023**, *55*, 857.

[44] M. He, J. H. Chen, A. J. Hu, Z. F. Yan, L. J. Cao, J. P. Long, *Energy Storage Mater.* **2023**, *62*, 102941.

[45] Q. P. Jian, T. S. Wang, J. Sun, M. C. Wu, T. S. Zhao, *Energy Storage Mater.* **2022**, *53*, 559.